Spectral Nonlinear Optical Response of Ion-Implanted Au and Ag Nanoparticles in Sapphire: A Three-Level Model Description

Domenico Genchi[●],[1] Raúl Rangel-Rojo[●],[2] Jhovani Bornacelli,[3] Alejandro Crespo-Sosa[●],[4]
Alicia Oliver[●],[4] and Tiziana Cesca[●][1,][*]

[1]*University of Padua, Department of Physics and Astronomy, NanoStructures Group (NSG), via Marzolo 8,*
I-35131 Padova, Italy

[2]*Departamento de Óptica, División Física Aplicada, CICESE, Ensenada, Baja California, México*

[3]*Sección de Estudios de Posgrado e Investigación, Escuela Superior de Ingeniería Mecánica y Eléctrica Unidad*
Zacatenco, Instituto Politécnico Nacional, Ciudad de México 07738, México

[4]*Instituto de Física, Universidad Nacional Autónoma de México, Apartado Postal 20-364, Mexico D.F. 01000,*
México

Nonlinear materials are of great technological interest for the realization of nanophotonic devices able to control and manipulate light. These properties can be specifically engineered by exploiting the surface plasmon resonance of plasmonic nanocomposites, in proximity of which nonlinear absorption and refraction are largely enhanced. An exploration of the spectral, irradiance, and host material dependence of the nonlinear parameters is important to be able to gain a thorough understanding of the nonlinear response. In the present work, we investigate the nonlinear optical response of Au and Ag nanoparticles embedded in sapphire by a spectral *z*-scan characterization across the localized surface plasmon band of the samples. We also present a comparison of the results obtained for Au nanoparticles embedded both in silica and in sapphire, produced under equivalent conditions, to test the influence of the host material. We theoretically describe the spectral trends of both the nonlinear absorption coefficient and nonlinear refractive index by implementing a three-level model, which provides important insights into the main physical parameters controlling the observed spectral features, and the possibility of *ab initio* composite designs with tailored properties.

I. INTRODUCTION

The study of the optical properties of nanostructured materials, specifically collections of nanoparticles embedded in some host material, has attracted considerable interest in the past few years [1–6]. This interest arises in the most part from the capability of tailoring their optical properties by manipulating their different fabrication parameters: composition, morphology, and the spatial distribution of the nanoparticles, as well as the dielectric contrast with the host medium. Their nonlinear optical properties are particularly interesting in order to implement different functionalities in proposed applications, such as saturable absorbers [7], nonlinear elements information processing systems [8], among others [9–11].

Metallic nanoparticles embedded in a dielectric matrix in particular have attracted a lot of attention, due to the capability of exciting localized surface plasmons, and the resonances associated with them. These metal-dielectric

composites display strong absorption bands in the visible arising from the localized surface plasmon resonances (LSPRs), producing different optical phenomena, such as a strong dichroism for example [3,12]. Regarding their nonlinear optical properties, it is well known that they are greatly enhanced on or near these LSPRs, resulting in relatively large nonlinear optical coefficients [2,13–17]. The degenerate third-order nonlinearity gives rise to nonlinear absorption and refraction, the latter being observed in different effects, such as self-focusing, self-modulation, and four-wave mixing [18]. This nonlinear response is of interest from the point of view of possible applications, provided that they have a strong enough response to make their use feasible. Applications such as all-optical switching rely on nonlinear refraction, while laser mode-locking relies on nonlinear absorption, for example. Most applications will involve waveguiding devices of some sort, so achievement of efficient waveguiding is of great importance. This has been demonstrated for the Ag nanoparticle-containing channel waveguides produced by masked ion implantation [19], a further step toward the implementation of devices. Being on or near

————————
*tiziana.cesca@unipd.it

a resonance usually implies an enhancement of the nonlinear coefficients, but this enhancement works differently for nonlinear absorption than for nonlinear refraction, which will have in general different wavelength dependencies. Because of this, it is important to conduct a detailed characterization of the spectral dependence of the nonlinear response of a given material, in order to understand the response and to identify possible interesting regimes for a given application. For example, a spectral region where nonlinear absorption becomes negligible while nonlinear refraction remains finite [20,21] is important for all-optical switching applications, since nonlinear absorption represents deleterious effects [22]. There have been many studies of the nonlinear response of nanostructured materials [23,24], but only a few include the spectral dependence of the nonlinear parameters [13,15,25–28].

Another aspect that has an important influence on the spectral position of the LSPRs, and more importantly on the magnitude of the nonlinear response, is the dielectric contrast with the host. This is characterized by the local field factor f_1, given by $f_1 = 3\epsilon_d/(\epsilon_m + 2\epsilon_d)$, where ϵ_d is the dielectric function of the dielectric host (purely real and positive for a transparent dielectric) and ϵ_m is the dielectric function of the metal, usually complex, with a negative real part. The effective third-order nonlinear susceptibility of the composite $\chi_{\text{eff}}^{(3)}$ is given by $\chi_{\text{eff}}^{(3)} = p|f_1|^2 f_1^2 \chi_m^{(3)} + \chi_d^{(3)}$ [29], where p is the volume filling fraction of the nanoparticles, and $\chi_m^{(3)}$ and $\chi_d^{(3)}$ are the third-order susceptibilities of the metal and dielectric, respectively. The contribution of the host susceptibility $\chi_d^{(3)}$ is usually orders of magnitude smaller than that of the metal, which is further amplified by the local field factor contribution, indicating that the response is actually dominated by the properties of the metal-dielectric metamaterial as a whole. In this sense, the dielectric contrast is another parameter that can be manipulated to improve the nonlinear response, and since the local field factor appears as the fourth power in the expression for the effective nonlinearity of the composite, a small change in this factor can have a strong impact on the size of the nonlinearity. It therefore makes sense to use a high refractive index dielectric (e.g., sapphire or titania) as the host to maximize this factor [29].

In this work, we present a detailed study of the nonlinear refraction and absorption observed in composites consisting of either gold or silver nanoparticles embedded in sapphire, and their spectral dependence across the LSPR absorption features. We also show results for Au nanoparticles embedded in silica under similar implantation conditions for comparison. For the case of Au, the opportunity to contrast the response for different host materials across an ample spectral region allows the study of the local field effect on the overall nonlinearity. The samples are produced by the ion-implantation technique, which allows good control of the concentration and size distribution of the nanoparticles, and due to the fact that

they are embedded, the long time stability of the samples is assured. The spectral trends of both the nonlinear absorption coefficient and nonlinear refractive index are theoretically described by implementing a three-level model. This model represents a simple, but very useful tool to get insights into the main physical parameters controlling the observed spectral features and to design nanocomposites with properly tailored nonlinear response.

II. EXPERIMENTAL PROCEDURES

A. Samples synthesis and characterization

Ion implantation is performed at room temperature using an implantation energy of 2 MeV at the 3MV tandem accelerator (NEC 9SDH-2 Pelletron) at the Instituto de Física, Universidad Nacional Autónoma de México. Ag and Au ions are implanted with a fluence of 2.5×10^{16} cm^{-2} in high-purity sapphire and silica plates. After metal ion implantation in sapphire, each sample is heated under a reducing atmosphere (RA, 50%N$_2$+50%H$_2$) for 90 min at a temperature of 950 °C, while for the Au-implanted silica sample, the thermal treatment is done in air at 1100 °C for 60 min. In the following the samples are named according to the implanted ion and the substrate, as Au:sapphire, Ag:sapphire, and Au:silica. The implantation fluence and the parameters of the implantation profile (projected range R_p below the sample's surface and the FWHM) are measured by Rutherford backscattering spectrometry (RBS). The results are shown in Table I.

The absorbance spectra of the thermally treated samples are measured using a Jasco V670 spectrophotometer. The spectral range between 200 and 900 nm has been explored. The absorbance spectra measured for each sample are reported in Fig. 1. The observed peaks correspond to the LSPR of the plasmonic nanoparticles. In particular, Au:sapphire and Au:silica have maximum absorbance at 561 and 525 nm, respectively, whereas Ag:sapphire exhibits a LSPR band centered at 464 nm. The particle size distribution for the samples studied in this work is estimated by performing simulations of the absorbance spectra according to Mie theory [30]. The size distribution for the Au:silica sample is Gaussian with a mean radius of about 3.8 nm and a standard deviation of 1.9 nm. For the Au and Ag nanoparticles implanted in sapphire, we instead had to use a wide size distribution that is not Gaussian. In particular, for the Au:sapphire sample, the radii

TABLE I. Projected range (R_p) and the FWHM of the ion-implantation profile of each sample.

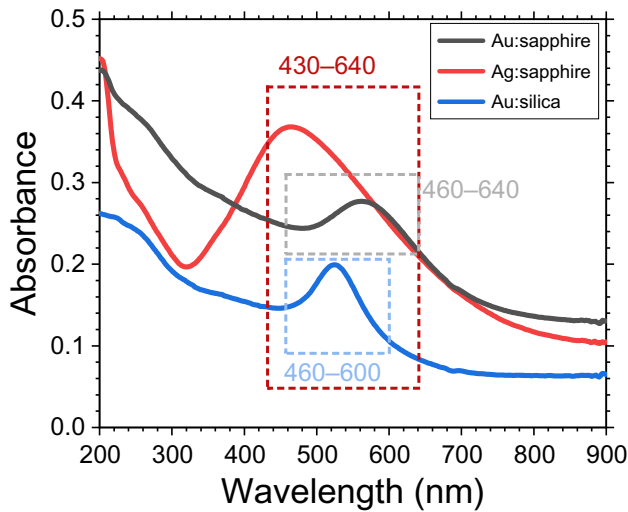| Substrate	Sapphire		Silica
Implanted ions	Au	Ag	Au
R_p (nm)	329	520	570
FWHM (nm)	187	251	282

FIG. 1. Absorbance spectra of the analysed samples. The dashed lines enclose the spectral ranges explored for each sample by the z-scan technique, i.e., the regions around the plasmon resonance peak of each sample.

range mainly from 5 to 35 nm, and there is also a significant number of particles with sizes less than 2 nm. For the Ag:sapphire sample, the radii range from 18 to 50 nm, also with a significant number of particles with size less than 2 nm. These results are in accordance with previous TEM and optical studies performed in similar samples with Au and Ag nanoparticles embedded in silica or sapphire at similar implantation energies and thermal annealing [30–32]. Moreover, it is possible to estimate a mean volumetric density ρ by choosing for each sample a mean particle radius r, the RBS measured implantation fluence, and the FWHM of the ion distribution [33]. We used a mean particle size of 3.8, 20, and 30 nm for the Au:silica, Au:sapphire, and Ag:sapphire samples, respectively, according to the Mie simulations. The volumetric density ρ and the mean volume of a nanoparticle in each sample allow us to roughly estimate a filling factor of 1.5%, 3.2%, and 2.2% for the Au:silica, Au:sapphire, and Ag:sapphire samples, respectively.

B. z-scan measurements

The nonlinear absorption coefficient β and the nonlinear refractive index n_2 of the investigated samples are determined by the single-beam z-scan technique [34–36]. A converging lens focuses the laser beam on the sample while the transmitted intensity is measured. The sample is translated along the beam propagation axis (z) so that the incident beam intensity varies with z, being maximum at the lens focus. The nonlinear response is detected as variations of the normalized transmittance. The z-scan measurements can be performed in two configurations, namely *open aperture* (OA) and *closed aperture* (CA).

In the former all the transmitted intensity is measured, whereas in the latter a small aperture in front of the detector partially cuts the transmitted beam, making the measure sensitive to phase distortions. From the analysis of the normalized OA and CA transmittance curves, β and n_2 can be extracted, respectively.

In this work, OA and CA measurements are performed simultaneously by using the following setup. The third harmonic beam of a mode-locked Nd:YAG laser ($\lambda = 355$ nm), supplying 18 ps pulses with 10 Hz repetition rate and an average pulse energy of approximately 7 mJ, is employed to pump an optical parametric amplifier (OPA), which tunes the beam wavelength in a wide spectral range between 420 and 2400 nm. The short pulse duration employed precludes the appearance of intrapulse thermal effects, while the low repetition rate prevents the possibility of cumulative pulse-to-pulse thermal processes, thus ensuring that the nonlinear response activated in the samples is purely electronic in origin. The incident beam has a TEM_{00} Gaussian profile with a beam waist of $w_0 = 38.6$ μm at $\lambda = 600$ nm, measured by the knife-edge method [37–39], and its intensity (I_0) can be varied by means of optical density filters. A beam splitter divides the incident beam so that on one arm its intensity is measured by a photodetector (reference signal) and on the other arm it is focused by a converging lens ($f = 200$ mm) on the sample, which is mounted on a 200-mm-long translation stage that moves it along the z direction, namely the laser beam propagation path. The transmitted beam is then split into the OA and CA branches: along the former the beam is directly focused onto a photodetector, whereas along the latter the beam first passes through an iris diaphragm, i.e., the aperture, and is then focused onto another photodetector. The linear transmittance of the aperture used in this work is $S = 0.29$. The signal revealed by the two detectors is normalized by the reference signal obtaining the OA transmittance (T_{OA}) and the CA transmittance (T_{CA}), respectively. The three photodetectors are connected to a digital oscilloscope and from it to a computer, which also allows us to control the OPA and the translation stage by remote. Each point of the z-scan curves is acquired by averaging 100 pulses. All the z scans are performed in the forward and backward directions to ensure that no artifacts due to local damage in the sample are induced in the z-scan curves.

The quantitative analysis of the OA and CA measurements, to determine the nonlinear absorption coefficient β and the nonlinear refractive index n_2, is done following the approach described in detail in Ref. [40]. To minimize the number of degrees of freedom and get a more reliable determination of the nonlinear coefficients, for all the measurements, the OA curve is first independently analyzed to extract the nonlinear absorption coefficient and then this is set into the fit function of the CA curve from which the nonlinear refractive index is obtained.

III. RESULTS AND DISCUSSION

A. Spectral response

The nonlinear optical properties of plasmonic nanocomposites are expected to be strong in the spectral region around their LSPR due to the enhancement of the local electric field in the plasmonic nanoparticles [16]. Hence, a spectral z-scan characterization of the nonlinear absorption (NLA) and nonlinear refraction (NLR) of the produced samples is performed in the spectral regions around the LSPR peak (λ_{LSPR}) of each sample. In particular, the ranges shown in the dashed regions in Fig. 1 are explored. The measurements are conducted with an average peak intensity at the lens focus of $I_0 \sim 5$ GW/cm^2. This value has been chosen in order to be sufficient for activating the samples nonlinearity and not excessive to prevent modification or damage of the samples.

1. Au:sapphire

As an example, in Fig. 2 we report the OA scans (upper panels) and the CA scans (lower panels) measured at three selected wavelengths corresponding to the LSPR peak ($\lambda = 560$ nm, central column) of the Au:sapphire sample and two opposite ends of the explored range ($\lambda = 480$ nm, left column and $\lambda = 620$ nm, right column). The red curves are the best fits obtained with the approach described in Ref. [40]. At 560 nm, which is exactly in correspondence with the maximum absorbance of the sample

(see Fig. 1), the sample exhibits strong saturable absorption (SA), which generates a peak of transmittance in the OA curve [Fig. 2(b)] at the focal point ($z = 0$) since the material becomes more transparent as the incident intensity increases. This corresponds to a negative nonlinear absorption coefficient ($\beta < 0$). At the same wavelength, clear nonlinear refraction is also observed in the CA transmittance curve [Fig. 2(e)]. The shape of the CA curve depends on the character of the NLR, i.e., on the sign of the nonlinear refractive index n_2. In the case of pure nonlinear refraction ($\beta = 0$), self-defocusing (SD, $n_2 < 0$) is represented by a transmittance curve showing a peak in the prefocal region and a valley in the postfocal region with an inflection point at $z = 0$; the opposite occurs in the case of self-focusing (SF, $n_2 > 0$) [34]. However, if the sample exhibits nonlinear absorption ($\beta \neq 0$), the CA scan is affected by both the NLA and NLR. This happens in the case of Au:sapphire at $\lambda = 560$ nm [Fig. 2(e)]; here, the CA curve shows a transmittance increase due to the NLA by approaching the focal position, and an asymmetric scan is generated, indicating SF. By spectrally moving far from the λ_{LSPR} of the sample, changes in the transmittance curves occur. At $\lambda = 480$ nm, namely on the left-hand side of the LSPR peak, the sample exhibits an opposite nonlinear absorption response, characterized by a minimum of transmittance close to the focal point [OA scan in Fig. 2(a)], characteristic of reverse saturable absorption (RSA) and thus of a positive nonlinear absorption coefficient ($\beta > 0$). Correspondingly, the CA scan [Fig. 2(d)]
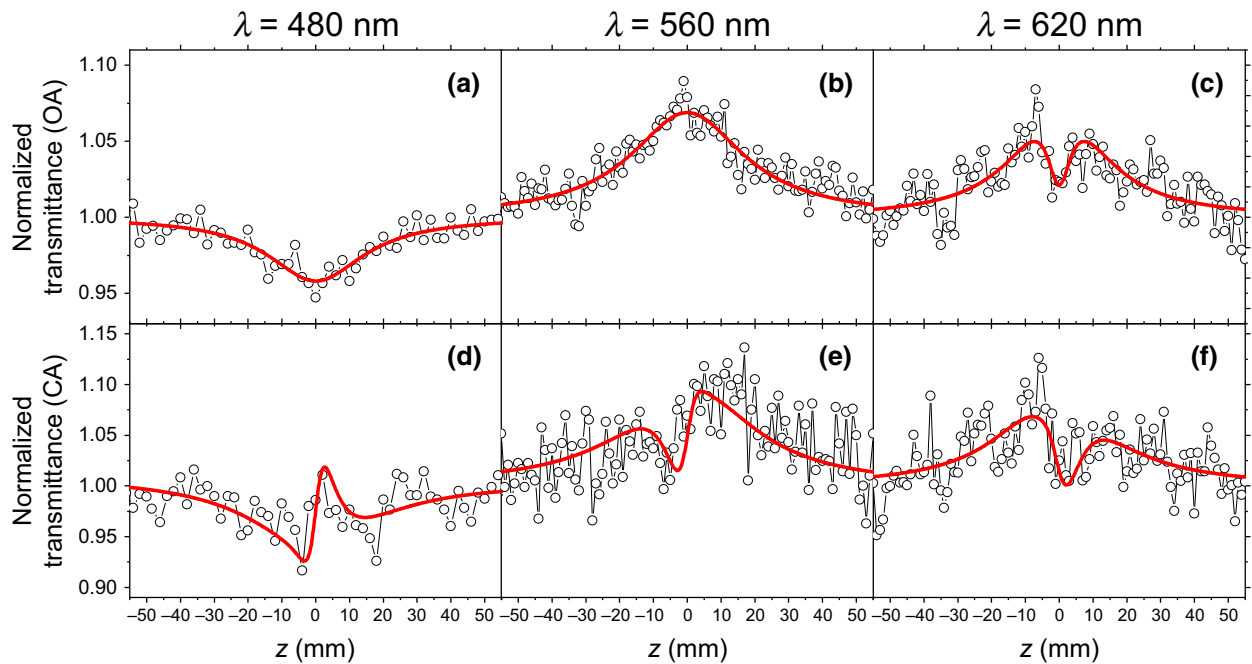

FIG. 2. (a)–(c) OA and (d)–(f) CA z-scan curves of Au:sapphire at the wavelengths indicated over the panels. The red solid lines are the best fits obtained in each scan. The measurements are performed with a beam intensity of the order of $I_0 = 5$ GW/cm^2 at the lens focal point (the exact values of I_0 for each scan are reported in Table II).

indicates a SF response. At $\lambda = 620$ nm, namely on the right-hand side of the LSPR peak, two opposite features in the OA scan can be observed [Fig. 2(a)]; here, the transmittance curve exhibits an increase before and after the focal position and a small valley at $z = 0$. The first feature is typical of SA, whereas the second corresponds to RSA. This indicates that two components of the NLA coefficient with opposite sign coexist and they are activated at different intensities; in fact, the intensity is maximum at the focal point and decreases going far from it, so that the nonlinear absorption coefficient becomes intensity dependent. In such a case, β cannot be simply described by a purely constant value, but the following expression can be employed, which also accounts for possible saturation effects of the nonlinear components [40,41]:

$$\beta(I) = \beta_{\mathrm{SA}}(I) + \beta_{\mathrm{RSA}}(I) = \frac{\beta_-}{1 + I/I_S^-} + \frac{\beta_+}{1 + I/I_S^+}. \quad (1)$$

Here β_- and β_+ are unsaturated NLA parameters, respectively, referring to SA and RSA, while I_S^- and I_S^+ are the

corresponding saturation intensities. By observing the CA curve at the same wavelength [Fig. 2(f)], a peak-valley feature can be noted, indicating in this case SD behavior.

Summarizing briefly, the above described z scans suggest that in the Au-implanted sapphire sample: (i) the NLA is larger near λ_{LSPR} and it decreases along the tails of the surface plasmon resonance band, where it changes its character; and (ii) a sign inversion of the nonlinear refractive index occurs by moving from λ_{LSPR} towards the red. To further assess this description we performed a detailed spectral characterization of the nonlinear optical parameters of the sample across its LSPR peak. The trends of β and n_2 as a function of the wavelength are displayed in the left column of Fig. 3 (central and bottom rows, respectively). In the upper row the absorbance spectrum of the sample is reported for comparison. The vertical dashed lines are used to indicate the spectral position of the LSPR peak (black line) and the wavelength at which the sign reversal of the nonlinear refractive index occurs (blue line). The red and blue solid lines are the spectral trends of β and n_2 simulated by means of the
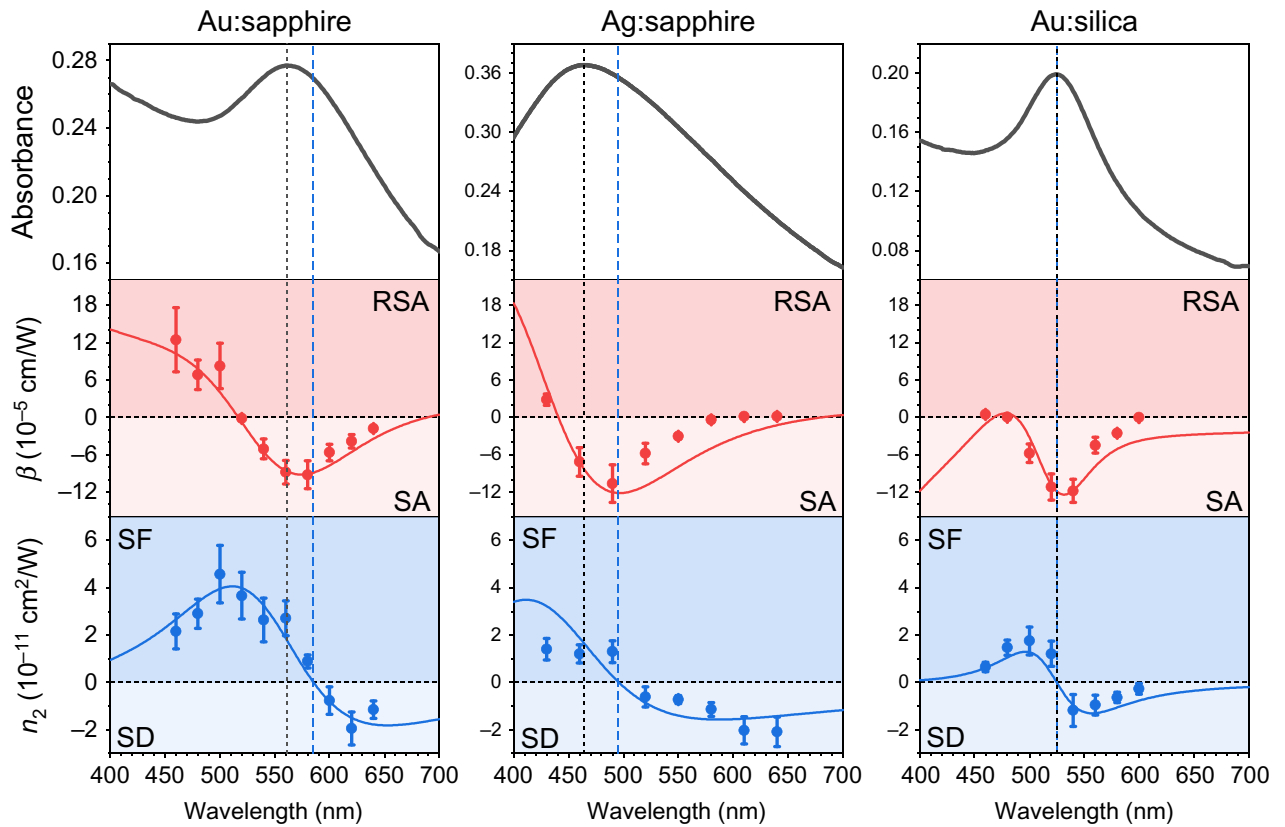

FIG. 3. Spectral trend of the nonlinear absorption coefficient β (central row) and the nonlinear refractive index n_2 (bottom row) of Au:sapphire (left column), Ag:sapphire (central column), and Au:silica (right column); the upper row shows absorbance spectra of the samples. In the central row, only the dominant component of β is displayed where β_- and β_+ coexist (see Table II). The red and blue solid curves represent the spectral trend of the corresponding nonlinear parameter simulated using the three-level model with the best-fit values. The vertical dashed lines indicate the spectral position of the LSPR peak (black) and of the sign reversal of n_2 (blue) determined by the simulations with the three-level model. The measurements are performed with a beam intensity of the order of $I_0 = 5$ GW/cm^2 at the lens focal point (the exact values of I_0 for each scan are reported in Table II).

TABLE II. Nonlinear optical parameters of the studied samples extracted from the *z*-scan measurements.

I_0 (GW/cm^2)	λ (nm)	α_0 (10^4 cm^{-1})	β_- (10^{-5} cm/W)	β_+ (10^{-5} cm/W)	I_S^- (GW/cm^2)	I_S^+ (GW/cm^2)	n_2 (10^{-11} cm^2/W)
			Au:sapphire				
2.1 ± 0.2	520	3.2 ± 0.2	-0.30 ± 0.06	...	...	...	16 ± 3
2.8 ± 0.3	560	3.4 ± 0.2	-5.9 ± 1.4	...	0.22 ± 0.06	...	4.3 ± 1.6
2.2 ± 0.2	600	3.2 ± 0.2	-5.8 ± 1.2	...	0.28 ± 0.06	...	-5.4 ± 2.4
3.9 ± 0.5	460	3.0 ± 0.2	...	13 ± 5	...	0.06 ± 0.03	2.2 ± 0.7
4.6 ± 0.8	480	3.0 ± 0.1	...	6.8 ± 2.4	...	0.13 ± 0.02	2.9 ± 0.6
3.7 ± 0.6	500	3.0 ± 0.2	...	8 ± 4	...	0.06 ± 0.02	4.6 ± 1.2
4.0 ± 0.7	520	3.2 ± 0.2	-0.16 ± 0.04	...	...	...	3.7 ± 1.0
4.7 ± 0.8	540	3.3 ± 0.2	-5.1 ± 1.6	...	0.22 ± 0.07	...	2.6 ± 0.9
3.8 ± 0.4	560	3.4 ± 0.2	-8.8 ± 1.9	...	0.17 ± 0.04	...	2.7 ± 0.7
5.1 ± 0.6	580	3.3 ± 0.2	-9.2 ± 2.2	...	0.19 ± 0.04	...	0.9 ± 0.3
6.0 ± 0.7	600	3.2 ± 0.2	-5.6 ± 1.3	...	0.40 ± 0.05	...	-0.8 ± 0.6
4.8 ± 0.5	620	2.9 ± 0.1	-3.8 ± 1.1	0.25 ± 0.09	0.5 ± 0.2	...	-1.9 ± 0.7
7.2 ± 0.7	640	2.7 ± 0.1	-1.8 ± 0.4	0.17 ± 0.04	0.9 ± 0.1	...	-1.1 ± 0.4
9.5 ± 1.0	520	3.2 ± 0.2	-1.7 ± 0.8	...	0.4 ± 0.2	...	-1.4 ± 0.4
10 ± 1	560	3.4 ± 0.2	-2.3 ± 0.4	...	0.7 ± 0.1	...	0.5 ± 0.2
11 ± 1	600	3.2 ± 0.2	-5.1 ± 1.0	...	0.35 ± 0.06	...	-0.4 ± 0.5
			Ag:sapphire				
1.6 ± 0.2	460	3.4 ± 0.2	-16 ± 3	...	0.13 ± 0.03	...	8.5 ± 1.5
2.3 ± 0.2	580	2.5 ± 0.1	...	0.17 ± 0.03	...	...	-2.1 ± 0.8
5.6 ± 0.6	430	3.2 ± 0.2	...	2.8 ± 0.9	...	0.3 ± 0.1	1.4 ± 0.5
6.6 ± 0.7	460	3.4 ± 0.2	-7.2 ± 2.3	...	0.11 ± 0.03	...	1.2 ± 0.4
5.5 ± 0.6	490	3.3 ± 0.2	-11 ± 3	...	0.13 ± 0.01	...	1.3 ± 0.5
5.4 ± 0.7	520	3.0 ± 0.2	-5.8 ± 1.7	...	0.22 ± 0.03	...	-0.6 ± 0.4
5.5 ± 0.5	550	2.8 ± 0.1	-3.0 ± 0.4	...	0.6 ± 0.1	...	-0.7 ± 0.2
4.3 ± 0.4	580	2.5 ± 0.1	-0.4 ± 0.4	0.06 ± 0.05	0.48 ± 0.05	...	-1.1 ± 0.3
4.1 ± 0.4	610	2.2 ± 0.1	...	0.12 ± 0.02	...	...	-2.0 ± 0.6
3.4 ± 0.4	640	1.9 ± 0.1	...	0.16 ± 0.02	...	...	-2.1 ± 0.6
14 ± 1	460	3.4 ± 0.2	-9 ± 6	0.04 ± 0.05	0.14 ± 0.08	...	0.9 ± 0.2
11 ± 1	580	2.5 ± 0.1	-0.4 ± 0.1	...	1.5 ± 0.5	...	0.18 ± 0.08
			Au:silica				
1.6 ± 0.2	480	1.27 ± 0.06	...	...	...	...	2.3 ± 0.7
1.8 ± 1.8	520	1.62 ± 0.08	-14 ± 4	...	0.08 ± 0.02	...	4.7 ± 1.2
1.7 ± 0.2	560	1.26 ± 0.06	-0.3 ± 0.09	...	...	...	-3.0 ± 0.9
6.0 ± 0.6	460	1.70 ± 0.08	...	0.4 ± 0.1	...	0.1 ± 0.4	0.6 ± 0.2
5.7 ± 0.6	480	1.80 ± 0.09	...	0.04 ± 0.01	...	...	1.5 ± 0.3
4.1 ± 0.4	500	2.0 ± 0.1	-5.8 ± 1.5	0.06 ± 0.02	0.12 ± 0.04	...	1.7 ± 0.6
4.8 ± 0.5	520	2.3 ± 0.1	-11 ± 2	...	0.10 ± 0.02	...	1.2 ± 0.5
4.2 ± 0.4	540	2.2 ± 0.1	-12 ± 2	...	0.11 ± 0.02	...	-1.2 ± 0.7
4.2 ± 0.4	560	1.78 ± 0.09	-4.5 ± 1.3	...	0.17 ± 0.05	...	-1.0 ± 0.4
5.3 ± 0.5	580	1.45 ± 0.07	-2.5 ± 0.4	...	0.17 ± 0.03	...	-0.6 ± 0.2
6.3 ± 0.7	600	1.22 ± 0.06	-0.04 ± 0.01	...	...	...	-0.3 ± 0.2
12 ± 1	480	1.80 ± 0.09	-0.09 ± 0.03	...	7 ± 5	...	0.2 ± 0.2
14 ± 1	520	2.3 ± 0.1	-1.1 ± 0.5	0.07 ± 0.03	1.2 ± 0.5	...	0.3 ± 0.1
12 ± 1	560	1.78 ± 0.09	-2.6 ± 0.4	...	0.36 ± 0.05	...	-0.2 ± 0.2

three-level model explained in Sec. III B. The numerical values of all the nonlinear parameters extracted from the performed *z*-scan analysis are collected in Table II. The nonlinear absorption coefficient (central row) shows an almost symmetrical trend with respect to the LSPR peak, having the largest absolute value near λ_{LSPR} (SA response) and gradually decreasing at the wavelengths along the peak tails. At wavelengths shorter than 520 nm the sample

exhibits a RSA behavior. Conversely, on the right tail of the peak, a positive component of the NLA coefficient appears at 620 nm, coexisting with the negative component (see Table II). Both components tend to vanish at longer wavelengths. The nonlinear refractive index (bottom row) exhibits the following trend: n_2 increases from 460 to 500 nm, where it takes the largest positive value (self-focusing behavior), then it decreases and changes its sign between 580 and 600 nm, assuming the most negative value (self-defocusing behavior) at 620 nm. It is interesting to note that in this sample the change in the nonlinear refraction response from SF to SD occurs in a wavelength range quite redshifted (of about 25 nm) with respect to its LSPR peak, i.e., in a region in which both the linear and nonlinear absorption properties of the sample start to decrease significantly.

2. Ag:sapphire

The spectral trend of the nonlinear optical response of Ag:sapphire is shown in the central column of Fig. 3. The numerical values of the NLA and NLR parameters estimated at all the explored wavelengths are summarized in Table II. The z scans obtained at 430, 490, and 640 nm are reported in Fig. 4. As in Au:sapphire, the Ag:sapphire sample exhibits a strong saturable absorber behavior ($\beta < 0$) close to the LSPR peak: at λ_{LSPR} the absolute value of β is even larger than that of Au:sapphire (consistently

with the stronger plasmonic properties of Ag with respect to Au). The SA character gradually decreases, moving towards the tails of the absorption band, where it turns to RSA ($\beta > 0$), as shown in Figs. 4(a) and 4(c). However, at $\lambda = 430$ nm the RSA response is much more pronounced and significantly saturated with respect to $\lambda = 640$ nm (see the values in Table II), owing to the proximity to the Ag interband transition region. Similarly to the Au:sapphire sample, in Ag:sapphire a sign reversal of n_2 is also observed, indicating a transition from self-focusing to self-defocusing. This occurs between 480 and 500 nm, i.e., at longer wavelengths with respect to the sample's LSPR peak (about 30 nm redshifted from it). As with the Au:sapphire sample, Ag:sapphire exhibits the strongest SF response on the left of the resonance peak. Moreover, by moving toward the red, we observe a gradual increase of $|n_2|$, which reaches its largest negative value ($n_2 = -2.1 \times 10^{-11}$ cm^2/W) at 640 nm. This means that also in this sample the transition from SF to SD occurs in a wavelength range in which correspondingly both the linear and nonlinear absorption start to decrease and a strong NLR response (SD type) is obtained where the NLA is almost null. This property is highly appealing for the implementation of these metallic nanocomposites in optical devices, e.g., for all-optical switching applications, where a major challenge is the maximization of NLR factors of merit, minimizing linear and nonlinear absorption [42,43].
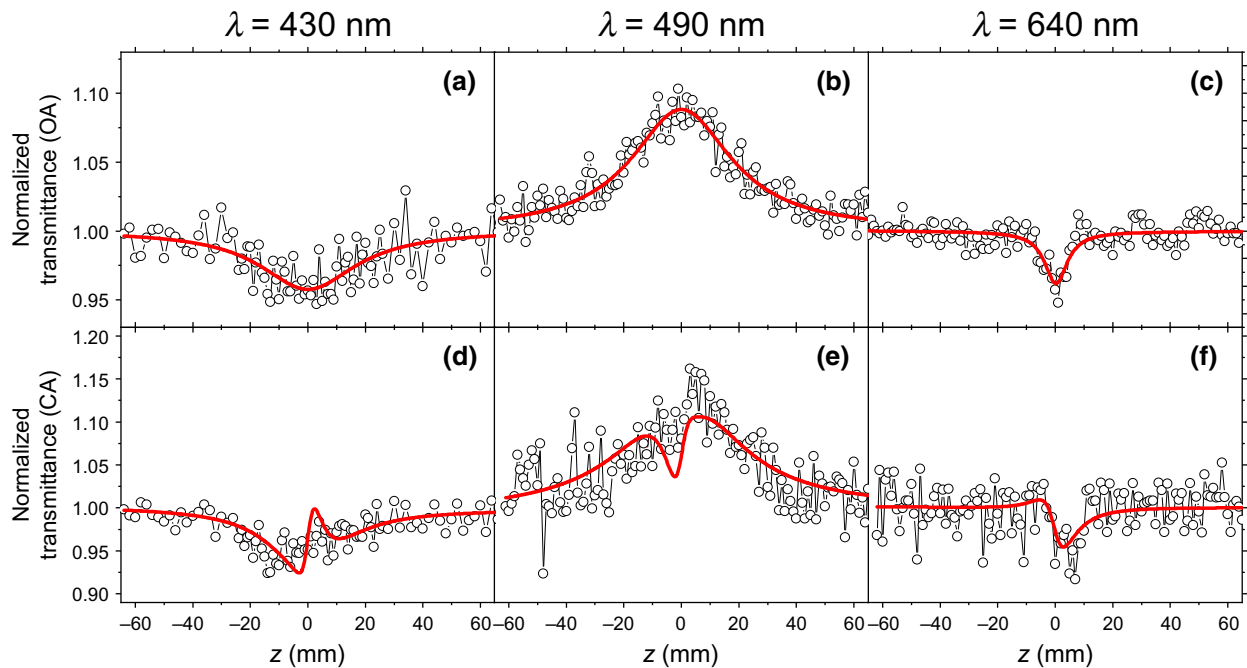

FIG. 4. (a)–(c) OA and (d)–(f) CA z-scan curves of Ag:sapphire at the wavelengths indicated over the panels. The red solid lines are the best fits obtained in each scan. The measurements are performed with a beam intensity of the order of $I_0 = 5$ GW/cm^2 at the lens focal point (the exact values of I_0 for each scan are reported in Table II).

3. Au:silica

In order to investigate the effect of the substrate and the dielectric contrast in the nonlinear optical response of these metallic nanocomposites, we also measured the spectral dependence of the nonlinear optical parameters of Au:silica (right column of Fig. 3 and Table II). The OA and CA scans measured at three selected wavelengths across the sample absorption band are shown in Fig. 5. Regarding the NLA properties, we find that the behavior of this sample is similar to that of the samples implanted in sapphire, again highlighting an enhancement of the nonlinear absorption coefficient near the LSPR peak, where the sample exhibits a strong saturable absorber character. Moreover, also in this case a change of sign in the nonlinear refractive index from positive (self-focusing) to negative (self-defocusing) values is observed by increasing the wavelength. Nonetheless, differently from what has been found for sapphire-based nanocomposites, here the sign inversion of n_2 occurs exactly in correspondence with the LSPR peak and the largest n_2 values are obtained in its close proximity (positive on the left-hand side of the LSPR peak and negative on the right-hand side). As a consequence, in this sample the strongest NLR response and the transition from SF to SD are obtained in a spectral region where at the same time both the linear and nonlinear absorption properties are the highest, thus placing major

limitations on the possible implementation of this kind of nanocomposite in optical devices.

B. Three-level model

It is important to have a model that can correctly explain the spectral dependence observed for the nonlinear response of the different samples. On the one hand, this can give an insight into the spectral regions that can be interesting for possible applications, and on the other hand, it can provide some *a priori* design capability of composite systems with tailored nonlinearities. There are different approaches that can be employed for such a model: one that has been applied successfully to explain the spectral [44] and irradiance dependencies [45,46] of different nanocrystalline and plasmonic materials considers the combination of ground- and excited-state absorption in a three-level system. Specifically, for the nanocomposites investigated in the present work, the first excited state corresponds to the LSPR of the nanoparticles and the second excited state is that responsible for the absorption features observed in the 200–250 nm region for all samples. These states have contributions from different processes, such as intraband transitions or hot electrons [16], all based on electronic excitation. Nonetheless, it has to be stressed that the details of the physical origin of theses processes are not relevant for the purpose of the implementation of this model, they
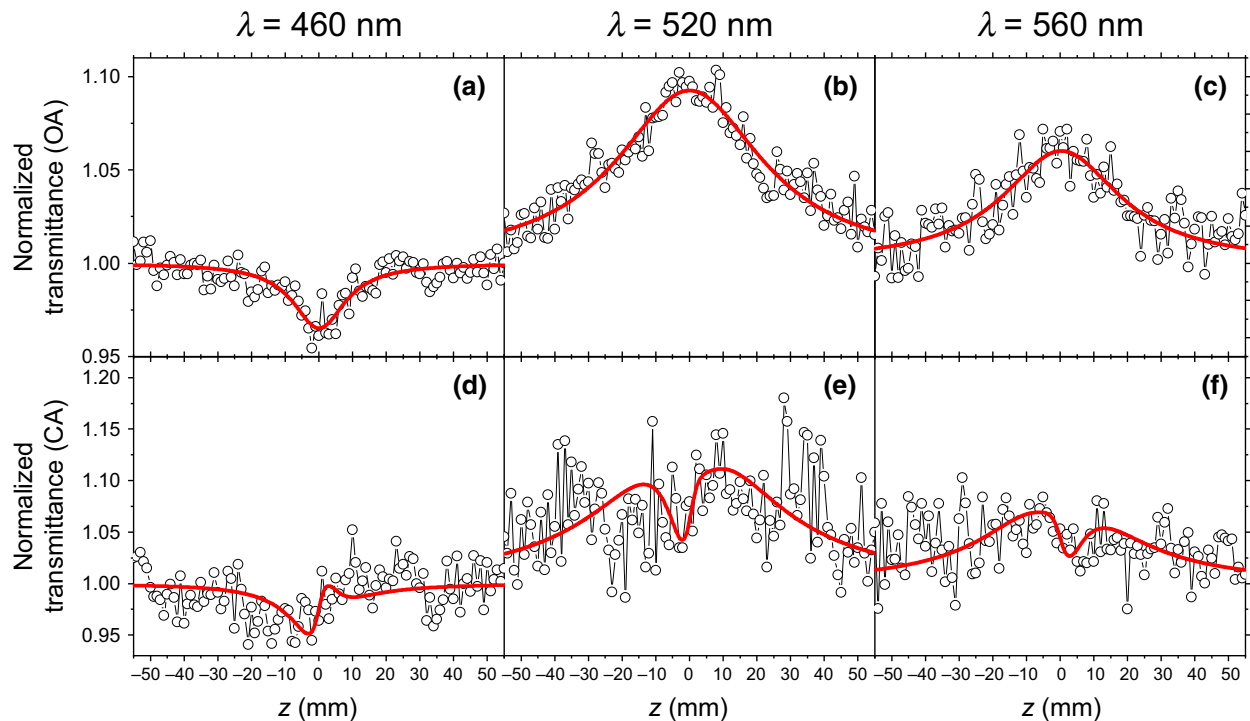

FIG. 5. (a)–(c) OA and (d)–(f) CA z-scan curves of Au:silica at the wavelengths indicated over the panels. The red solid lines are the best-fits obtained in each scan. The measurements have been performed with a beam intensity on the order of $I_0 = 5$ GW/cm^2 at the lens focal point (the exact values of I_0 for each scan are reported in Table II).

only matter in the sense that they give origin to the absorption features observed. The model is used with different variants; in the present case we consider direct transitions from the ground state $|1\rangle$ to states $|2\rangle$ and $|3\rangle$, depending on the excitation wavelength, and the excited-state $|2\rangle \rightarrow |3\rangle$ absorption is also considered; decay from level $|3\rangle$ is considered to happen only into level $|2\rangle$ for simplicity. Under these assumptions, we can write the rate equations for the populations N_i of the involved three states as

$$\frac{dN_1}{dt} = (N_2 - N_1)p\sigma_{12} + \frac{N_2}{\tau_{21}} - (N_1 - N_3)p\sigma_{13}, \quad (2)$$

$$\frac{dN_2}{dt} = -(N_2 - N_1)p\sigma_{12} - \frac{N_2}{\tau_{21}} - (N_2 - N_3)p\sigma_{23} + \frac{N_3}{\tau_{32}}, \quad (3)$$

$$\frac{dN_3}{dt} = (N_2 - N_3)p\sigma_{23} - \frac{N_3}{\tau_{32}} + (N_1 - N_3)p\sigma_{13}, \quad (4)$$

where τ_{ji} is the $|j\rangle \rightarrow |i\rangle$ decay time, σ_{ij} is the absorption cross section for the $|i\rangle \rightarrow |j\rangle$ transition, and $p = I/\hbar\omega$

is the photon flux. The steady-state solution for the rate equations, $dN_i/dt = 0$ (under the constriction that $N_0 = N_1 + N_2 + N_3$ at all times), can be used to calculate an effective susceptibility χ_{eff} with real and imaginary parts given by [21,45,47]

$$\text{Im}(\chi_{\text{eff}}) = \frac{n_0 c}{\omega}[(N_1 - N_2)\sigma_{12} + (N_2 - N_3)\sigma_{23} + (N_1 - N_3)\sigma_{13}], \quad (5)$$

$$\text{Re}(\chi_{\text{eff}}) = \frac{n_0 c}{\omega}[(N_1 - N_2)(\omega_{21} - \omega)\sigma_{12}T_2 + (N_2 - N_3)(\omega_{32} - \omega)\sigma_{23}T_3 + (N_1 - N_3)(\omega_{31} - \omega)\sigma_{13}T_3], \quad (6)$$

where $\omega_{ji} = (E_j - E_i)/\hbar$ is the resonance frequency of the $|i\rangle \rightarrow |j\rangle$ transition, while T_2 and T_3 are the dephasing times of the $|2\rangle$ and $|3\rangle$ levels, respectively. Solving Eqs. (2)–(4) and substituting into Eqs. (5) and (6) we obtain

$$\text{Im}(\chi_{\text{eff}}) = \frac{N_0 n_0 c}{\omega} \frac{p[\sigma_{12}\sigma_{23}(W_{21} + W_{32}) + \sigma_{13}\sigma_{23}W_{32}] + W_{21}W_{32}(\sigma_{12} + \sigma_{13})}{3p^2\sigma_{23}(\sigma_{12} + \sigma_{13}) + p[(2\sigma_{12} + \sigma_{13})W_{32} + (2\sigma_{13} + \sigma_{23})W_{21}] + W_{21}W_{32}}, \quad (7)$$

$$\text{Re}(\chi_{\text{eff}}) = \frac{N_0 n_0 c}{\omega}$$
$$\times \left\{ \frac{p[\sigma_{12}\sigma_{23}(\Delta_{21}T_2W_{21} + \Delta_{32}T_3W_{32}) + \sigma_{13}\sigma_{23}(\Delta_{32}T_3(W_{32} - W_{21}) + \Delta_{31}T_3W_{21})] + (\sigma_{12}\Delta_{21}T_2 + \sigma_{13}\Delta_{31}T_3)W_{21}W_{32}}{3p^2\sigma_{23}(\sigma_{12} + \sigma_{13}) + p[(2\sigma_{12} + \sigma_{13})W_{32} + (2\sigma_{13} + \sigma_{23})W_{21}] + W_{21}W_{32}} \right\}, \quad (8)$$

with $\Delta_{ji} = \omega_{ji} - \omega$ being the detuning factors of each $|i\rangle \rightarrow |j\rangle$ transition. Besides, we have used the decay rates $W_{ji} = 1/\tau_{ji}$ and we have considered the fact that σ_{12} $\sigma_{13} \approx 0$, i.e., there is no overlap in the absorption cross sections for the transitions to the two excited states. This result can be connected to the usual expansion of the polarization in terms of powers of E in order to obtain the third-order susceptibility $\chi^{(3)}$. For a centrosymmetric system, this can be written as

$$P = \varepsilon_0\chi^{(1)}E + \varepsilon_0\chi^{(3)}E^3 + \cdots$$
$$= \varepsilon_0(\chi^{(1)} + \chi^{(3)}E^2)E = \varepsilon_0\chi_{\text{eff}}E. \quad (9)$$

In this way, $\chi^{(3)}$ can be calculated by expanding χ_{eff} in powers of I and keeping the term that is linear with I. This

is done for both the real and imaginary parts of χ_{eff}, giving

$$\text{Im}(\chi^{(3)}) = \frac{\varepsilon_0 c^2 n_0^2 N_0}{2\hbar\omega^2 W_{32}W_{21}}[-2\sigma_{12}^2 W_{32} - \sigma_{13}^2(W_{32} + 2W_{21}) + \sigma_{13}\sigma_{23}(W_{32} - W_{21}) + \sigma_{12}\sigma_{23}W_{32}], \quad (10)$$

$$\text{Re}(\chi^{(3)}) = \frac{\varepsilon_0 c^2 n_0^2 N_0}{2\hbar\omega^2 W_{32}W_{21}}[-2\sigma_{12}^2 W_{32}\Delta_{21}T_2$$
$$- \sigma_{13}^2\Delta_{31}T_3(W_{32} + 2W_{21})$$
$$+ \sigma_{13}\sigma_{23}\Delta_{32}T_3(W_{32} - W_{21})$$
$$+ \sigma_{12}\sigma_{23}W_{32}\Delta_{32}T_3]. \quad (11)$$

Here, the frequency dependence is contained in the different σ_{ij} cross sections that can be written in terms of

the actual lineshapes $g_{ji}(\omega)$, which we consider to be Lorentzians as

$$\sigma_{ij} = \frac{\pi n_0 \omega \mu_{ij}^2}{\varepsilon_0 c \hbar} g_{ji(\omega)} = \frac{\pi n_0 \omega \mu_{ij}^2}{\varepsilon_0 c \hbar} \frac{\gamma_{ij}/2\pi}{(\omega - \omega_{ji})^2 + (\gamma_{ij}/2)^2}. \tag{12}$$

The expressions for $\mathrm{Re}(\chi^{(3)})$ and $\mathrm{Im}(\chi^{(3)})$ can be simplified by introducing the reduced parameters $\mu_{13}^r \equiv \mu_{13}^2/\mu_{12}^2$, $\mu_{23}^r \equiv \mu_{23}^2/\mu_{12}^2$, and $\tau_r \equiv \tau_{32}/\tau_{21}$; then

$$\mathrm{Im}(\chi^{(3)}) = \frac{\pi^2 n_0^4 N_0 \tau_{21} \mu_{12}^4}{2\hbar^3 \varepsilon_0} \{-2g_{21}^2(\omega) - (\mu_{13}^r)^2 g_{31}^2(\omega)(1 + 2\tau_r) + \mu_{23}^r g_{32}(\omega)[g_{21}(\omega) + \mu_{13}^r g_{31}(\omega)(1 - \tau_r)]\}, \tag{13}$$

$$\mathrm{Re}(\chi^{(3)}) = \frac{\pi^2 n_0^4 N_0 \tau_{21} \mu_{12}^4 T_2}{2\hbar^3 \varepsilon_0} \left\{ -2g_{12}^2(\omega)\Delta_{21} - (\mu_{13}^r)^2 g_{13}^2(\omega)\Delta_{31}\left(\frac{T_3}{T_2}\right)(1 + 2\tau_r) + \mu_{13}^r g_{32}(\omega)\Delta_{32}\left(\frac{T_3}{T_2}\right)[g_{21}(\omega) \right.$$

$$\left. + \mu_{13}^r g_{31}(\omega)(1 - \tau_r)] \right\}. \tag{14}$$

The experimental results are described in terms of the nonlinear absorption and refraction parameters β and n_2, which are related to $\chi^{(3)}$ by [18]

$$\beta = \frac{4\pi}{\lambda \varepsilon_0 n_0^2 c} \mathrm{Im}(\chi^{(3)}) \tag{15}$$

and

$$n_2 = \frac{1}{\varepsilon_0 n_0^2 c} \mathrm{Re}(\chi^{(3)}). \tag{16}$$

Equations (13) and (14) can then be used to fit the spectral dependence for the NLA and NLR of the studied materials. To this end, the following procedure is followed. First, the linear absorption spectra are fitted to the sum of two Lorentzians to obtain ω_{21} and ω_{31}, and the actual lineshapes $g_{21}(\omega)$ and $g_{31}(\omega)$. From these, $\omega_{32} = \omega_{31} - \omega_{21}$ is also obtained. The experimental $\beta(\omega)$ data are then fitted using μ_{13}^r, μ_{23}^r, and τ_r as fitting parameters. This set of parameters is then used to fit the $n_2(\omega)$ data, for which the ratio T_3/T_2 is now the only free parameter.

In Fig. 3 we show the fits obtained for the three studied samples using the described procedure, with the fitting parameters collected in Table III. From the experimental data in Fig. 3, the nonlinear absorption coefficient β

is negative on resonance, and has a minimum (maximum $|\beta|$) very close to the resonant peak for the three samples. For the Au:sapphire and Ag:sapphire samples, however, β becomes positive above resonance, i.e., short wavelengths. For a material with a single isolated absorption feature, the nonlinear absorption is given only by the term $-g_{21}^2(\omega)$ in the expression for $\mathrm{Im}(\chi^{(3)})$, with a minimum exactly at resonance, and should remain negative across the whole resonant regime. The three-level model reproduces very well the change to positive values for β at short wavelengths, which is explained by the effect of excited-state absorption on the nonlinear response.

For the nonlinear refractive index n_2 also shown in Fig. 3, all three samples show negative values below resonance (longer wavelengths), changing to positive above resonance. Again, for an isolated transition, $\mathrm{Re}(\chi^{(3)})$ would originate from the term $-g_{21}^2(\omega)\Delta_{21}$ and would change sign exactly at resonance. This is pretty much the case for the Au:silica sample, and it is very well reproduced by the model. For the Au:sapphire sample, and more markedly for the Ag:sapphire sample, this change of sign occurs at wavelengths below resonance. The model reproduces these features reasonably well, which again can be attributed to the influence of excited-state absorption on the nonlinear response. This shift that happens for the sample where the nanoparticles are embedded in sapphire, but

TABLE III.   Three-level model fitting parameters.

Sample	λ_{21} (nm)	λ_{31} (nm)	λ_{32} (nm)	μ_{13}^r	μ_{23}^r	τ_r	T_3/T_2
Au:silica	525	250	477	11 ± 2	3.15 ± 0.05	0.75 ± 0.05	$0.10 \pm 0.06 \times 10^{-2}$
Au:sapphire	565	202	314	8 ± 3	9.00 ± 0.03	0.05 ± 0.04	$7 \pm 2 \times 10^{-2}$
Ag:sapphire	467	203	359	1.0 ± 0.5	4.0 ± 0.1	1.0 ± 0.7	$20 \pm 6 \times 10^{-2}$

not for the one where silica is the host, has to do with the narrower LSPR features observed in the latter. This makes the influence of the higher-lying state less prominent, i.e., the LSPR acts more like an isolated absorption feature. Although the fits involve many parameters, we have found that the wavelength at which β changes sign depends strongly on the value of the μ_{23}^r ratio, while the equivalent crossing point for n_2 is strongly determined by the T_3/T_2 ratio. Hence, we have assigned small uncertainties to these two parameters in Table III. Variations of the other fitting parameters are seen to have a smaller impact on the features of the fits, and their uncertainties are accordingly considerably larger. Another important effect that can be observed from contrasting the results for the Au:sapphire and Au:silica samples is that the overall nonlinear refractive index n_2 is larger for the former by a factor of approximately 4. This is consistent with a larger local field factor f_1 for the high index sapphire, as compared to silica, resulting in a larger $\chi_{\text{eff}}^{(3)}$. A completely quantitative assessment of the influence of the host is difficult to establish, since although the implantation conditions for both host materials are the same, the nanoparticles nucleation processes are bound to be slightly different, resulting

in different size and depth distributions. Such a comparison cannot be made for measurements made at only one wavelength, because the resonance conditions will be quite different for the different hosts, which has a strong effect on the magnitude of the nonlinearity.

C. Intensity-dependent response

To get deeper insights into the nonlinear optical properties of the produced nanocomposites and to determine the conditions for getting the best performances, we also investigate the intensity dependence of their nonlinear response. The results are summarized in Fig. 6.

The measurements are performed for laser peak intensity values I_0 of 2, 5, and 10 GW/cm^2 (the exact intensity values are reported in Table II) at selected wavelengths across the LSPR peak of each sample. For the three investigated samples, the data clearly show a progressive fading of the nonlinear optical parameters when increasing the peak intensity. This is particularly evident for the nonlinear refractive index n_2 (left column in Fig. 6), and as a consequence it entails a decrease of the spectral contrast; at low intensities a much stronger difference in the NLR response (in both sign and amplitude) can be obtained by changing the wavelength.

IV. CONCLUSIONS

Nanocomposites made up of Au or Ag nanoparticles embedded in sapphire have been synthesized by ion implantation. Their nonlinear optical response has been spectrally investigated by the z-scan technique across the LSPR absorption peak of each sample. An intense nonlinear absorption coefficient ($\beta \sim 10^{-5}$ cm/W) is observed in correspondence of the surface plasmon resonance peak and a large nonlinear refractive index ($n_2 \sim 10^{-11}$ cm^2/W) is obtained in a spectral range where the linear and nonlinear absorption features are weaker. It is worth underlining that a regime where n_2 remains finite while nonlinear absorption becomes negligible constitutes a regime that is particularly interesting for all-optical switching applications, for which nonlinear absorption can be a deleterious effect. Moreover, for Au nanoparticles, the results show an overall enhancement factor of approximately 4 for the nonlinear refractive index when sapphire is the host material, over the case where silica is used. This enhancement, observable only through measurements across the whole resonance, is consistent with the expected influence of the dielectric contrast on the nonlinear response of the composite. The spectral results have been well reproduced theoretically by implementing a three-level model, which highlighted the role of excited-state absorption in determining the observed spectral features. The model represents a very useful tool to design nanocomposites with properly tailored nonlinearities for specific applications in different spectral ranges. It has been applied in the past to
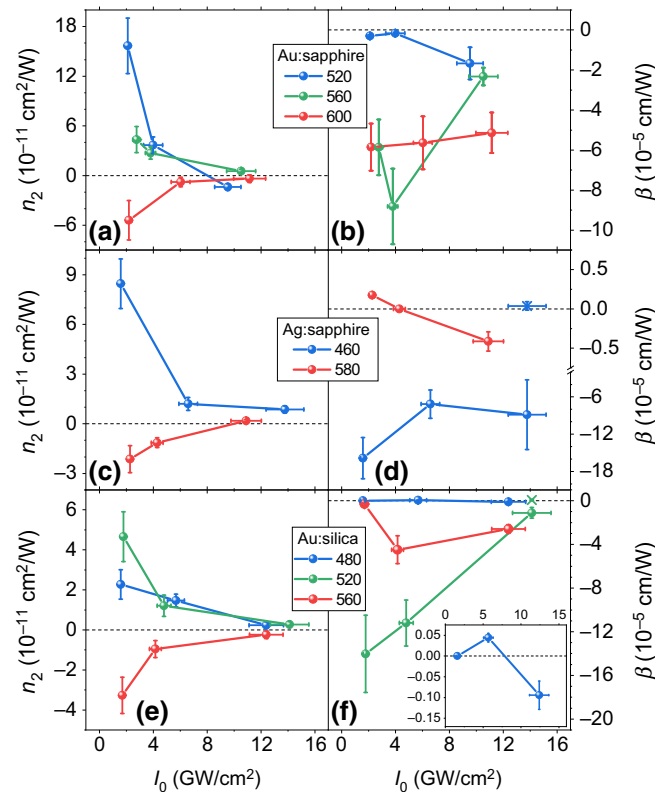

FIG. 6. Nonlinear refractive index n_2 (left) and nonlinear absorption coefficient β (right) of the three samples (Au:sapphire, Ag:sapphire, and Au:silica) as a function of the laser peak intensity I_0. For each sample, the measurements are performed at the wavelengths indicated in the legends.

study different aspects of the nonlinear response of a variety of nanostructured materials, such as organic nanocrystals in suspension, ordered arrays of metallic nanoprisms, and here for metallic nanoparticles embedded in glass, demonstrating its applicability in many kinds of different systems. The study of the intensity dependence of the nonlinear response shows that, for wavelengths where either n_2 or β changes sign, the response shows the coexistence of two weak effects of opposite signs. Finally, a complete study of the nonlinear response of the nanocomposites, such as the one presented here, is important in order to get a good understanding of the nonlinear response, in conjunction with a working model.

ACKNOWLEDGMENTS

[1] G. Mattei, P. Mazzoldi, and H. Bernas, in *Materials Science with Ion Beams* (Springer, Springer-Verlag Berlin Heidelberg, 2010), p. 287.

[2] R. Li, C. Pang, Z. Li, and F. Chen, Plasmonic nanoparticles in dielectrics synthesized by ion beams: Optical properties and photonic applications, Adv. Opt. Mater. **8,** 1902087 (2020).

[3] R. Rangel-Rojo, H. Sánchez-Esquivel, B. Can-Uc, A. Crespo-Sosa, and A. Oliver, in *Metal Nanostructures for Photonics* (Elsevier, Amsterdam, Netherlands, 2019), p. 39.

[4] T. Cesca, M. Manca, N. Michieli, and G. Mattei, Tuning the linear and nonlinear optical properties of ordered plasmonic nanoarrays by morphological control with thermal annealing, Appl. Surf. Sci. **491,** 67 (2019).

[5] E. Trave, M. Back, E. Cattaruzza, F. Gonella, F. Enrichi, T. Cesca, B. Kalinic, C. Scian, V. Bello, C. Maurizio, and G. Mattei, Control of silver clustering for broadband Er^{3+} luminescence sensitization in Er and Ag co-implanted silica, J. Lumin. **197,** 104 (2018).

[6] T. Cesca, N. Michieli, B. Kalinic, I. G. Balasa, R. Rangel-Rojo, J. A. Reyes-Esqueda, and G. Mattei, Bidimensional ordered plasmonic nanoarrays for nonlinear optics, nanophotonics and biosensing applications, Mater. Sci. Semicond. Process. **92,** 2 (2019).

[7] T. Zhang, Y. Sun, Y. Niu, and C. Liu, Enhanced nonlinear absorption of Au nanoparticles embedded into Nd:YAG crystal towards saturable absorber application, Appl. Phys. Express **12,** 122014 (2019).

[8] M. A. Camacho, A. K. Kar, B. S. Wherrett, M. Bakarezos, R. Rangel-Rojo, S. Yamada, H. Matsuda, H. Kasai, and H. Nakanishi, All-optical switching potentiality in Fabry-Perot devices containing poly-DCHD, Opt. Commun. **251,** 376 (2005).

[9] G. Ledoux, J. Gong, F. Huisken, O. Guillois, and C. Reynaud, Photoluminescence of size-separated silicon nanocrystals: Confirmation of quantum confinement, Appl. Phys. Lett. **80,** 4834 (2002).

[10] Q. Wang, S. Li, J. Qiao, R. Jin, Y. Yu, and S. Gao, CdS-CdSe (CdTe) core-shell quantum dots sensitized TiO_2 nanotube array solar cells, Solar Energy Mater. Solar Cells **132,** 650 (2015).

[11] H. Inouye, K. Tanaka, I. Tanahashi, T. Hattori, and H. Nakatsuka, Ultrafast optical switching in a silver nanoparticle system, Jpn. J. Appl. Phys. **39,** 5132 (2000).

[12] T. Cesca, E. Vianey García-Ramírez, H. Sánchez-Esquivel, N. Michieli, B. Kalinic, J. Manuel Gómez-Cervantes, R. Rangel-Rojo, J. Alejandro Reyes-Esqueda, and G. Mattei, Dichroic nonlinear absorption response of silver nanoprism arrays, RSC Adv. **7,** 17741 (2017).

[13] R. Sato, M. Ohnuma, K. Oyoshi, and Y. Takeda, Experimental investigation of nonlinear optical properties of ag nanoparticles: Effects of size quantization, Phys. Rev. B **90,** 125417 (2014).

[14] R. Sato, S. Ishii, T. Nagao, M. Naito, and Y. Takeda, Broadband plasmon resonance enhanced third-order optical nonlinearity in refractory titanium nitride nanostructures, ACS Photonics **5,** 3452 (2018).

[15] P. Ferrari, S. Upadhyay, M. V. Shestakov, J. Vanbuel, B. De Roo, Y. Kuang, M. Di Vece, V. V. Moshchalkov, J.-P. Locquet, P. Lievens, and E. Janssens, Wavelength-dependent nonlinear optical properties of ag nanoparticles dispersed in a glass host, J. Phys. Chem. C **121,** 27580 (2017).

[16] B. Palpant, in *Challenges and Advances in Computational Chemistry and Physics* (Springer, Netherlands, 2006), p. 461.

[17] D. Miu and I. Nicolae, Third order nonlinear optical properties of gold/alumina multilayer nanocomposites with different nanoparticle arrangements, Thin Solid Films **697,** 137829 (2020).

[18] R. W. Boyd, *Nonlinear Optics* (Academic Press, San Diego, CA USA, 2008), 3rd ed.

[19] B. Can-Uc, R. Rangel-Rojo, H. Márquez, L. Rodríguez-Fernández, and A. Oliver, Nanoparticle containing channel waveguides produced by a multi-energy masked ion-implantation process, Opt. Express **23,** 3176 (2015).

[20] R. Rangel-Rojo, S. Yamada, H. Matsuda, H. Kasai, Y. Komai, S. Okada, H. Oikawa, and H. Nakanishi, Refractive third-order nonlinearity in vanadium-oxide phthalocyanine microcrystals, Jpn. J. Appl. Phys. Part 1 **7,** 69 (1999).

[21] J. Bolger, T. G. Harvey, W. Ji, A. K. Kar, S. Molyneux, B. S. Wherrett, D. Bloor, and P. Norman, Near-resonant third-order optical nonlinearities in p-toluene sulfonate polydiacetylene, JOSA B **9,** 1552 (1992).

[22] H. Sánchez-Esquivel, K. Y. Raygoza-Sánchez, R. Rangel-Rojo, E. Gemo, N. Michieli, B. Kalinic, J. A. Reyes-Esqueda, T. Cesca, and G. Mattei, Spectral dependence of nonlinear absorption in ordered silver metallic nanoprism arrays, Sci. Rep. **7,** 5307 (2017).

[23] Y.-X. Zhang and Y.-H. Wang, Nonlinear optical properties of metal nanoparticles: A review, RSC Adv. **7,** 45129 (2017).

[24] R. A. Ganeev, Characterization of the optical nonlinearities of silver and gold nanoparticles, Opt. Spectrosc. **127,** 487 (2019).

[25] B. Zhang, R. Sato, H. Momida, T. Ohno, M. Chundak, M. Naito, M. Yoshitake, and Y. Takeda, Spectral dependence of the third-order optical susceptibility of Au

nanostructures: Experiments and first-principles calculations, Phys. Rev. B **100**, 035446 (2019).

[26] R. Sato, M. Ohnuma, K. Oyoshi, and Y. Takeda, Spectral investigation of nonlinear local field effects in Ag nanoparticles, J. Appl. Phys. **117**, 113101 (2015).

[27] L. D. Boni, E. C. Barbano, T. A. d. Assumpcão, L. Misoguti, L. R. P. Kassab, and S. C. Zilio, Femtosecond third-order nonlinear spectra of lead-germanium oxide glasses containing silver nanoparticles, Opt. Express **20**, 6844 (2012).

[28] Y. Hamanaka, A. Nakamura, N. Hayashi, and S. Omi, Dispersion curves of complex third-order optical susceptibilities around the surface plasmon resonance in Ag nanocrystal-glass composites, JOSA B **20**, 1227 (2003).

[29] B. Can-Uc, R. Rangel-Rojo, A. Peña-Ramírez, C. B. de Araújo, H. T. M. C. M. Baltar, A. Crespo-Sosa, M. L. Garcia-Betancourt, and A. Oliver, Nonlinear optical response of platinum nanoparticles and platinum ions embedded in sapphire, Opt. Express **24**, 9955 (2016).

[30] P.-E. Mota-Santiago, A. Crespo-Sosa, J.-L. Jiménez-Hernández, H.-G. Silva-Pereyra, J.-A. Reyes-Esqueda, and A. Oliver, Size characterisation of noble-metal nano-crystals formed in sapphire by ion irradiation and subsequent thermal annealing, Appl. Surf. Sci. **259**, 574 (2012).

[31] H. G. Silva-Pereyra, J. Arenas-Alatorre, L. Rodriguez-Fernández, A. Crespo-Sosa, J. C. Cheang-Wong, J. A. Reyes-Esqueda, and A. Oliver, High stability of the crystalline configuration of Au nanoparticles embedded in silica under ion and electron irradiation, J. Nanopart. Res. **12**, 1787 (2010).

[32] J. Bornacelli, C. Torres-Torres, H. G. Silva-Pereyra, G. J. Labrada-Delgado, A. Crespo-Sosa, J. C. Cheang-Wong, and A. Oliver, Superlinear photoluminescence by ultrafast laser pulses in dielectric matrices with metal nanoclusters, Sci. Rep. **9**, 5699 (2019).

[33] J. Bornacelli, C. Torres-Torres, B. Can-Uc, R. Rangel-Rojo, and A. Oliver, Plasmon coupling interactions and inhibition of nonlinear absorption in a complex system with Ag and Pt nanoparticles in silica, Appl. Opt. **59**, D69 (2020).

[34] M. Sheik-Bahae, A. Said, T.-H. Wei, D. Hagan, and E. V. Stryland, Sensitive measurement of optical nonlinearities using a single beam, IEEE J. Quantum Electron. **26**, 760 (1990).

[35] E. V. Stryland, M. Sheik-Bahae, A. Said, and D. Hagan, Characterization of nonlinear optical absorption and refraction, Prog. Cryst. Growth Charact. Mater. **27**, 279 (1993).

[36] P. B. Chapple, J. Staromlynska, J. A. Hermann, T. J. Mckay, and R. G. Mcduff, Single-beam z-scan: Measurement techniques and analysis, J. Nonlinear Opt. Phys. Mater. **06**, 251 (1997).

[37] J. A. Arnaud, W. M. Hubbard, G. D. Mandeville, B. de la Clavière, E. A. Franke, and J. M. Franke, Technique for fast measurement of gaussian laser beam parameters, Appl. Opt. **10**, 2775 (1971).

[38] J. M. Khosrofian and B. A. Garetz, Measurement of a gaussian laser beam diameter through the direct inversion of knife-edge data, Appl. Opt. **22**, 3406 (1983).

[39] M. A. de Araújo, R. Silva, E. de Lima, D. P. Pereira, and P. C. de Oliveira, Measurement of gaussian laser beam radius using the knife-edge technique: Improvement on data analysis, Appl. Opt. **48**, 393 (2009).

[40] T. Cesca, P. Calvelli, G. Battaglin, P. Mazzoldi, and G. Mattei, Local-field enhancement effect on the nonlinear optical response of gold-silver nanoplanets, Opt. Express **20**, 4537 (2012).

[41] T. Cesca, N. Michieli, B. Kalinic, A. Sánchez-Espinoza, M. Rattin, V. Russo, V. Mattarello, C. Scian, P. Mazzoldi, and G. Mattei, Nonlinear absorption tuning by composition control in bimetallic plasmonic nanoprism arrays, Nanoscale **7**, 12411 (2015).

[42] M. Samoć, Third-order nonlinear optical materials: Practical issues and theoretical challenges, J. Mol. Model. **17**, 2183 (2010).

[43] M. Samoc, K. Matczyszyn, M. Nyk, J. Olesiak-Banska, D. Wawrzynczyk, P. Hanczyc, J. Szeremeta, M. Wielgus, M. Gordel, L. Mazur, R. Kolkowski, B. Straszak, M. P. Cifuentes, and M. G. Humphrey, in *Organic Photonic Materials and Devices XIV*, edited by C. Tabor, F. Kajzar, T. Kaino, and Y. Koike (SPIE OPTO, San Francisco, USA, 2012).

[44] R. Rangel-Rojo, H. Matsuda, H. Kasai, and H. Nakanishi, Irradiance dependence of the resonant nonlinearities in an organic material, J. Opt. Soc. Am. B **17**, 1376 (2000).

[45] R. Rangel-Rojo, S. Yamada, H. Matsuda, H. Kasai, H. Nakanishi, A. K. Kar, and B. S. Wherrett, Spectrally resolved third-order nonlinearities in polydiacetylene microcrystals: Influence of particle size, J. Opt. Soc. Am. B **15**, 2937 (1998).

[46] H. Sánchez-Esquivel, K. Y. Raygoza-Sánchez, R. Rangel-Rojo, N. Michieli, B. Kalinic, T. Cesca, and G. Mattei, Ultra-fast dynamics in the nonlinear optical response of silver ordered nanoprisms arrays, Nanoscale **10**, 5182 (2018).

[47] A. Yariv, *Quantum Electronics* (Wiley, New York, USA, 1989), 3rd ed., Chap. 8.